International Journal of Nanomedicine

Dovepress
open access to scientific and medical research

Open Access Full Text Article

ORIGINAL RESEARCH

# Melt Electrowriting Combined with Fused Deposition Modeling Printing for the Fabrication of Three-Dimensional Biomimetic Scaffolds for Osteotendinous Junction Regeneration

Shengshan Ma[1,2,*], Suyang Zheng[1,*], Dong Li[3], Wenhao Hu[4], Liming Wang[1]

[1]Department of Orthopedic Surgery, Nanjing First Hospital, Nanjing Medical University, Nanjing, Jiangsu, People's Republic of China; [2]Department of Sports Medicine, Lianyungang Clinical College of Nanjing Medical University, Lianyungang, Jiangsu, People's Republic of China; [3]Department of Trauma Center, The Affiliated Changzhou No.2 People's Hospital of Nanjing Medical University, Changzhou, Jiangsu, People's Republic of China; [4]Department of Orthopedic Surgery, The Affiliated Huai'an No.1 People's Hospital of Nanjing Medical University, Huai'an, Jiangsu, People's Republic of China

*These authors contributed equally to this work

Correspondence: Liming Wang, Department of Orthopedic Surgery, Nanjing First Hospital, Nanjing Medical University, 68 Changle Road, Nanjing, Jiangsu, People's Republic of China, Tel +86-25-5227-1000, Fax +86-25-5226-9924, Email wlmnjsy@163.com



**Purpose:** This study aims to explore a novel scaffold for osteotendinous junction regeneration and to preliminarily verify its osteogenic and tenogenic abilities in vitro.

**Methods:** A polycaprolactone (PCL) scaffold with aligned and orthogonal fibers was created using melt electrowriting (MEW) and fused deposition modeling (FDM). The scaffold was coated with Type I collagen, and hydroxyapatite was carefully added to separate the regions intended for bone and tendon regeneration, before being rolled into a cylindrical shape. Human adipose-derived stem cells (hADSCs) were seeded to evaluate viability and differentiation. Scaffold characterization was performed with Scanning Electron Microscope (SEM). Osteogenesis was assessed by alkaline phosphatase (ALP) and Alizarin red staining, while immunostaining and transcription-quantitative polymerase chain reaction (RT-qPCR) evaluated osteogenic and tendogenic markers.

**Results:** Scaffolds were developed in four variations: aligned (A), collagen-coated aligned (A+C), orthogonal (O), and mineral-coated orthogonal (O+M). SEM analysis confirmed surface morphology and energy-dispersive X-ray spectroscopy (EDS) verified mineral coating on O+M types. Hydrophilicity and mechanical properties were optimized in modified scaffolds, with A+C showing increased tensile strength and O+M improved in compression. hADSCs demonstrated good viability and morphology across scaffolds, with O+M scaffolds showing higher cell proliferation and osteogenic potential, and A and A+C scaffolds supporting tenogenic differentiation.

**Conclusion:** This study confirms the potential of a novel PCL scaffold with distinct regions for osteogenic and tenogenic differentiation, supporting the regeneration of osteotendinous junctions in vitro.

**Keywords:** tendon-bone healing, biomimetic, electrospun scaffold, near-field direct writing, tissue engineering

## Introduction

Tendon injuries, particularly at the tendon-bone junction, are increasingly common health issues that impose significant socio-economic burdens.[1] Injuries such as rotator cuff tears, patellar tendonitis, ligament tears, and Achilles tendonitis are prevalent.[2] For instance, rotator cuff injuries affect 30% of the US population over 60, with over 600,000 surgeries performed annually.[3,4] Post-surgical re-tear rates for tendon-bone interface repairs remain high, ranging from 20–94%, attributable to the limitations in fully reconstructing the innate architecture and biomechanics of tendon-bone junction, leading to a compromised repair strength.[5]

Received: 15 November 2023
Accepted: 28 March 2024
Published: 6 April 2024

The tendon-bone junction, also named osteotendinous junction, tendon-bone interface or tendon-bone insertion, is a specialized structure where calcified and non-calcified collagen fibers facilitate efficient force transmission and reduce stress concentrations.[6,7] Direct reattachment of tendon to bone is crucial for functional recovery, but healing this interface is challenging due to the need to integrate two different tissue types.[8] Healing and regeneration of the graded transitional zone are slow in both experimental and clinical settings.[9,10] Past attempts to enhance tendon-bone healing, including bone substitutes, periosteal autografts, growth factors, gene therapy, physical stimulation, and stem cell transplantation, have been met with limited success, failing to regenerate the natural graded transitional zone.[11]

In adult tendon repair, healing often results in scarring and tissue disorganization, unlike the regenerative processes observed in fetal tissues that heal without scar formation.[12,13] Despite advances in medical treatments focusing on reducing scarring, they fall short of achieving regenerative healing.[14] Research indicates that while both adult and late gestational fetal tendons heal with complications such as collagen disarray and adhesions, mid-gestational fetal tendons demonstrate superior healing capabilities.[14] This suggests an inherent regenerative capacity in fetal tendons that is not solely dependent on the in fetal environment, as evidenced by the maintained regenerative properties of fetal tendons when transplanted into adult organisms.[15] Consequently, this indicates the possibility of achieving scarless regeneration in adult tendons.

To enhance tendon-bone interface healing, a variety of strategies have been explored, including the use of bone-inductive growth factors, periosteum or polymer wraps, stem cell therapy, and tissue-engineered scaffolds.[3,16–18] Among these, bioresorbable scaffolds populated with stem cells show significant potential for enhanced repair at the tendon-bone interface.[5,19] Current research is concentrated on tissue engineering methods aimed at mimicking the scar-free fetal healing environment within scaffolds. This involves designing scaffolds that simulate the physiological conditions conducive to tissue regeneration.[20] Adipose-derived stem cells (ADSCs) are favored for seeding these scaffolds due to their versatility in differentiating into multiple cell lineages, their relative ease of collection, their abundance, and their low immunogenic profile, making them well-suited for promoting tendon-bone healing in an adult setting.[21,22]

To replicate the unique fibrous structure of the tendon-bone junction, often compared to a "toothbrush" pattern, scaffolds must be fabricated with fibers oriented both unidirectionally and in multiple directions. Such scaffolds need to be both biocompatible and biodegradable, providing initial structural integrity which subsequently allows for natural degradation within the body. Melt electrowriting (MEW) utilizing polycaprolactone (PCL) offers a precise method for fabricating fibers with these specifications.[23] PCL is an optimal choice for constructing accurate fibers due to its lower melting point, suitable rheology for extrusion, and robust mechanical characteristics.[23] It is also preferred in tissue engineering for its compatibility with biological tissues and its ability to degrade over time, which has been proven effective for tendon-bone integration in vitro studies.[19,24,25]

In this study, we fabricated a scaffold using MEW with PCL, with collagen I coating on tendonous area and hydroxyapatite coating on osteogenesis part. Physicochemical properties of the scaffold were characterized and osteogenic and tenogenic abilities were tested in vitro, to assess the feasibility of the scaffold for tendon-bone junction regeneration in-vivo.

# Materials and Methods

## Scaffold Fabrication

### Scaffold Printing

In this investigation, a multifunctional extrusion-based 3D printer (BP6601, EFL, China) was utilized to fabricate the scaffold. The material of choice for the scaffold was PCL particles (CAPA6800, Perstorp, UK), characterized by a melting temperature of 60 °C and a molecular weight of 80,000 $g \cdot mol^{-1}$. The printing parameters were set under ambient conditions at 25°C. The barrel temperature was maintained at 65°C, while the nozzle temperature was regulated at 85°C. During the MEW mode, an extrusion air pressure of 8 kPa was applied, alongside a voltage of 4.7 kV. The distance between the nozzle and the platform was set at 2.5 cm, with a printing speed of 1600 mm/min. In the fused deposition modeling (FDM) mode, the extrusion air pressure was increased to 450 kPa, and the printing speed was adjusted to 100 mm/min.

The pattern for MEW printing was created and encoded into G-code by the EFL-PotatoE software, which is specifically designed to accompany the 3D printer (Figure 1A and B). The process commenced with the fabrication of a single-layer framework using the FDM mode, which produced a structure with an approximate diameter of 250 μm, as shown in Figure 1C. Following this, the MEW mode was activated to deposit fibers, achieving a controllable diameter within the range of 5–10 μm, while preserving a uniform inter-fiber spacing of 150 μm. The MEW mode was used to print a 20-layer membrane structure that precisely matched the dimensions of the initial framework. The membrane was divided into two distinct regions: one comprising unidirectional fibers and the other featuring orthogonal fibers (Figure 1D).

## Scaffold Surface Modification

To enhance cell adhesion and promote cell differentiation capabilities, surface modification treatments were performed on the scaffold. The entire fiber surface of the scaffold was coated with type I collagen, while the orthogonal fiber area was additionally overlaid with hydroxyapatite through a mineralization process. Specifically, a 0.5% type I collagen-acetic acid solution was prepared using type I collagen (Sigma) and acetic acid solution (Sigma). The composite thin-layer scaffold was immersed in this solution for 3 hours and subsequently subjected to freeze-drying to achieve type I collagen (Col1)-coated fibers (Figure 1E). Following this, a 10% gelatin (Sigma) solution was prepared and used to envelop the well-aligned fibers (Figure 1F). The scaffold was then submerged in a simulated body fluid (SBF) solution at tenfold concentration, with sodium bicarbonate added to adjust the pH to approximately 6.5. The scaffold was allowed to rest undisturbed for 3 hours, facilitating the deposition and robust anchoring of hydroxyapatite onto the scaffold (Figure 1G).

Upon retrieval of the scaffold from the aforementioned solutions, it was immersed in a water bath maintained at 50°C to facilitate the dissolution of gelatin. This step aimed to remove the hydroxyapatite that had mineralized on the unidirectional fiber area. After the dissolution process, the scaffold underwent freeze-drying, ultimately resulting in a structure where the orthogonal fiber region was simultaneously coated with Col1 and hydroxyapatite, as depicted in Figure 1H.

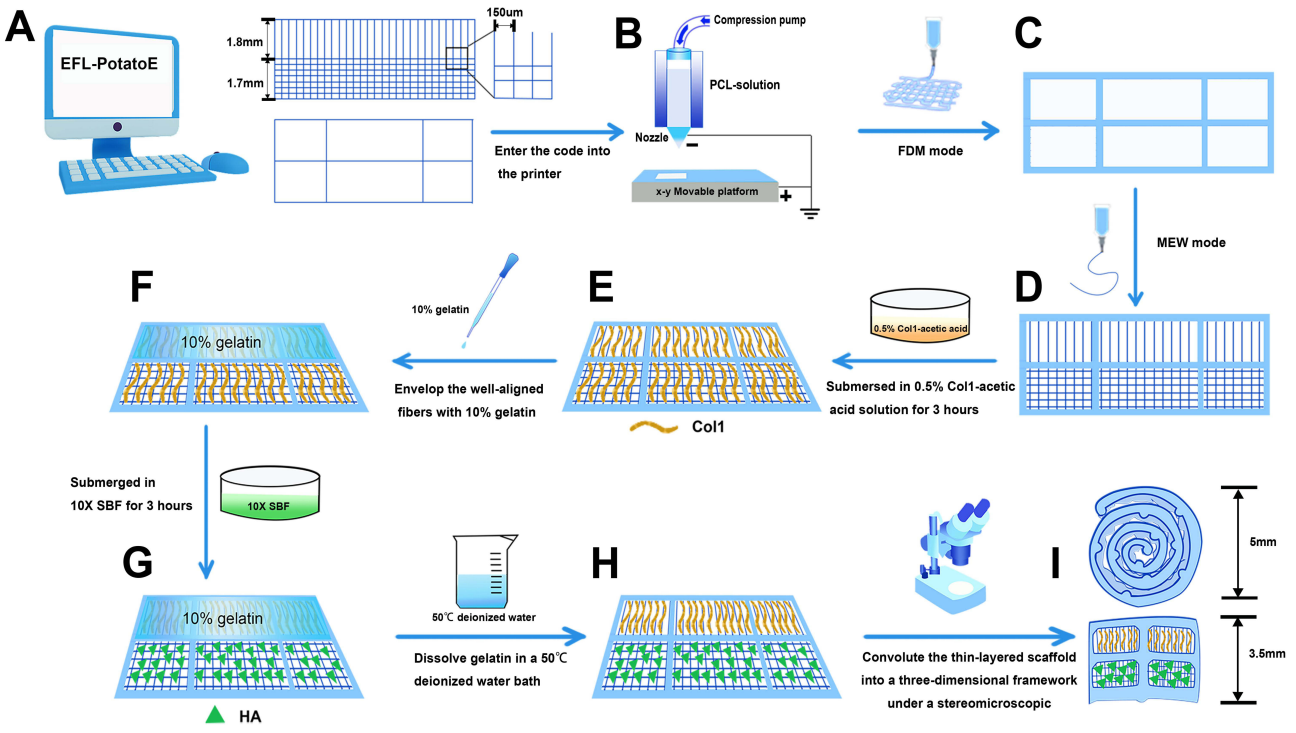


**Figure 1** Schematic illustration of the preparation of the biomimetic scaffold. (**A**) Monolayer scaffold structure designed using the EFL-PotatoE software. (**B**) Schematic of the 3D printer. (**C**) External framework printed in FDM mode. (**D**) Nano-microfibers generated in MEW mode. (**E**) Nano-microfibers coated with Col1. (**F**) 10% gelatin envelop the well-aligned fibers. (**G**) Orthogonal fibers coated with HA. (**H**) Different sections of the thin-layered scaffold coated with Col1 and HA, respectively. (**I**) Schematic illustration of the three-dimensional scaffold.

**Abbreviations**: Col1, type I collagen; SBF, simulated body fluid; HA, hydroxyapatite; FDM, fused deposition modeling; MEW, melt electrowriting.

### Three-Dimensional Configuration of the Scaffold

Utilizing stereomicroscopic visualization, the initially flat membranous scaffold was delicately rolled into a three-dimensional cylindrical framework, achieving a diameter of 5 mm and a height of 3.5 mm, as depicted in Figure 1I. To prepare for cellular cultivation, the scaffold was subjected to a comprehensive sterilization protocol, which entailed an overnight submersion in 75% ethanol and a subsequent period of ultraviolet light irradiation to ensure aseptic conditions.

## Scaffold Characterization

### Morphological Observation and Elemental Analysis

The structure of the fibers was examined using scanning electron microscopy (SEM) (Regulus 8100, Hitachi, Japan) at a voltage boost of 5 kV. The elemental composition of the scaffold was determined using energy dispersive spectroscopy (EDS). For improved electron conductivity and better SEM image clarity, samples were carefully placed on aluminum stubs and coated with a thin gold layer before imaging. ImageJ software was used to gauge the fiber diameter from the SEM photos. Additionally, the arrangement of the fibers was assessed based on these SEM images.

The images were processed using the OrientationJ plug-in within the ImageJ software to ascertain the directional orientation of the fibers. Initially, SEM images were converted to 8-bit grayscale. Utilizing the analysis function of the OrientationJ plug-in, fibers with varying orientations were distinctly color-coded. Subsequently, angular data from all fibers within the image were harvested and integrated into the Origin software. This software then portrayed the angular distribution in a polar coordinate system, enabling a comprehensive analysis of the fibers' orientation.

### Mechanical Property Assessment

The tensile and compressive characteristics of the scaffolds were assessed using the mechanical testing apparatus (Jitai-5kn, Jimtec, China). Each sample encountered a consistent 5 mm/min speed while undergoing unidirectional tension or compression. The stress-strain curves yielded data on vital parameters such as ultimate tensile and compressive strengths.

### Porosity Measurement

A volumetric approach was adopted to ascertain the scaffold's porosity:

$$\text{Porosity} = \frac{\text{scaffold volume} - \text{total fiber volume}}{\text{scaffold volume}}$$

Wherein:

$$\text{Scaffold volume} = \text{base area} \times \text{height}$$

$$\text{Total fiber volume} = \text{volume of a single fiber} \times \text{aggregate fiber count}$$

### Hydrophilicity Assessment

The hydrophilicity of the scaffolds was gauged by evaluating the water contact angle. This was executed using the water contact angle measurement instrument (JY-82C, Dingsheng, China). A droplet size of 16 microliters was used. The entire process was video-monitored with image frames captured at 50-ms intervals.

## Characterization of Scaffold-Mediated Tendon-Bone Healing in vitro

### hADSCs Seeding on Scaffolds

Human adipose-derived stem cells (hADSCs) from the American Type Culture Collection (PCS-500-011, ATCC) were expanded in a specialized mesenchymal stem cell medium (MM101-01, TransGen, China). The cells were cultured at 37°C in an environment with 5% $CO_2$. The medium was refreshed every three days, and the cells were passaged upon reaching 80% confluence. Prior to seeding, cells in the logarithmic growth phase were digested and centrifuged after the digestion was halted with fetal bovine serum and then resuspended in the mesenchymal stem cell medium to achieve a concentration of $6\times10^5$ cells/mL. For seeding, a negative pressure adsorption technique was employed, utilizing a custom-made simple device created from a modified pipette tip in conjunction with a pipettor to immerse the scaffold

in the cell suspension. After 24 hours of seeding, the scaffolds were transferred to Dulbecco's Modified Eagle's Medium (DMEM) supplemented with 10%fetal bovine serum (FBS).

### Scanning Electron Microscopy of Cell-Seeded Scaffolds

At three days post-seeding, the scaffolds with adherent cells were fixed in a 0.25% glutaraldehyde solution for a period of 24 hours. They were then washed three times with phosphate-buffered saline (PBS). The fixation process continued with the samples being immersed in a 1% osmic acid solution for one hour, followed by another set of three PBS washes. A stepwise dehydration was performed using incremental ethanol concentrations. After dehydration, the samples were mounted on aluminum stubs, sputter-coated with gold to make them conductive, and finally observed under a scanning electron microscope to assess cell attachment and morphology.

### Cytotoxicity and Cell Viability Assessment

Scaffolds were seeded with $5\times10^5$ hADSCs and cultured in DMEM containing 10% FBS. Cell viability and potential cytotoxic effects of various scaffolds were evaluated using a Calcein/PI Cell Viability/Cytotoxicity Assay Kit (C2015L, Beyotime, China). Following seeding, cells were incubated on scaffolds for a set duration before being washed once with sterile PBS. The cells were then incubated with the prepared Calcein AM/PI solution for 30 minutes at 37°C. Live and dead cells were distinguished based on their fluorescent staining patterns, which were visualized using a laser confocal scanning microscope (FV1000, OLYMPUS, Japan).

The proliferation rate and cytotoxicity of the hADSCs on the scaffolds were further determined using the CCK-8 assay kit (C0038, Beyotime, China). Cells were harvested from the scaffolds on days 1, 3, and 7 of culture and transferred to 96-well plates. They were then incubated in a 10% CCK-8 solution for 1 hour at 37°C in a 5% $CO_2$ atmosphere. The optical density of the culture medium was measured at a wavelength of 450 nm to quantify cell proliferation.

### Osteogenic Differentiation via ALP and Alizarin Red Staining

The osteogenic potential of hADSCs cultured on scaffolds was assessed using alkaline phosphatase (ALP) and alizarin red staining techniques. After a 28-day cultivation period, the scaffolds were fixed with 4% paraformaldehyde. They were then stained with a 2% (w/v) alizarin red solution (R23120, Bioon, China) for 10 minutes, followed by thorough rinsing with distilled water to remove excess dye. The stained scaffolds were examined under a fluorescence microscope in bright-field mode, and images were captured for documentation.

For semi-quantitative assessment of mineral deposition, alizarin red-stained specimens were processed with a 10% cetylpyridine chloride solution (IC5410, Solarbio, China) for one hour with gentle agitation at room temperature. The dye extract was then placed into a 96-well plate, and the absorbance was measured at 562 nm to quantify the mineralized nodules.

To quantitatively determine ALP activity, an alkaline phosphatase assay kit (P0321M, Beyotime, China) was utilized on days 14 and 28. The hADSCs on the scaffolds were lysed with the cell lysis buffer (P0013J, Beyotime, China) and subsequently homogenized. The lysed cell mixture was centrifuged, and the supernatant was collected in a 96-well plate. Detection buffer and color-developing substrate were added, and the mixture was incubated at 37°C for 30 minutes. The reaction was terminated using the provided stop solution, and the absorbance was recorded at 405 nm to evaluate ALP activity. The visualization of ALP activity in hADSCs cultured on scaffolds was performed using the Kaplow's/Azo Coupling Method provided by the alkaline phosphatase stain kit (G1480, Solarbio, China). After staining, the scaffolds were examined using the bright-field setting of a fluorescence microscope.

### Cytoskeleton and Protein Marker Visualization

Cytoskeletal organization and the expression of proteins indicative of osteogenic and tenogenic differentiation were assessed at various time points post-seeding. On days 1 and 10, the cellular cytoskeleton was stained with phalloidin, while on day 14, differentiation markers of cells seeded on the scaffolds were detected by immunofluorescence staining.

The procedure began with fixing the cells on the scaffolds using a 4% (v/v) formalin solution at room temperature for 10 minutes. Subsequently, the samples underwent three washes with ice-cold PBS. Permeabilization was achieved by treating the scaffolds with 0.1% Triton X-100 in PBS for 10 minutes. To prevent non-specific binding of antibodies, the cells were incubated in a 3% BSA solution for 30 minutes. The scaffolds were then incubated with diluted primary

antibodies overnight at 4°C. The following day, after three PBS washes to remove unbound primary antibodies, the samples were incubated with appropriate secondary antibodies for one hour at room temperature in the dark to avoid photobleaching. Post-incubation, the scaffolds were washed thrice in PBS under dark conditions. Nuclei were counter-stained using 4',6-diamidino-2-phenylindole (DAPI). The stained scaffolds were then examined, and images were captured using a laser confocal scanning microscope to analyze the organization of the cytoskeleton and the presence of differentiation markers, providing insight into the phenotypic progression of the hADSCs on the scaffolds. Three images were extracted from each time point and subgroup for analytical purposes. All image processing was undertaken using ImageJ software.

The primary antibodies used in this study comprised the following:

- Rabbit monoclonal [EPR7785] to collagen I (ab138492, abcam) (1:200)
- Rabbit monoclonal [EPR14334] to Runx2 (ab192256, abcam) (1:500)
- Rabbit polyclonal to SCXA (ab58655, abcam) (1:200)
- Rabbit monoclonal to TNC (A18156, ABclonal antibody) (1:200)

The secondary antibodies employed were CoraLite488/594-conjugated goat anti-rabbit IgG (H+L).

### RT-qPCR Analysis of Gene Expression

Gene expression profiling associated with osteogenic and tenogenic differentiation in hADSCs was carried out using reverse transcription-quantitative polymerase chain reaction (RT-qPCR). With an initial seeding density of $5\times10^5$ cells per scaffold, hADSCs were cultivated on custom-designed scaffolds in basal medium. The gene targets for osteoblastic differentiation included Runt-related transcription factor 2 (*Runx2*) and osteocalcin (*Ocn*), while tendon lineage genes of interest were tenomodulin (*Tnmd*), tenascin-C (*Tnc*), and scleraxis (*Scx*).

Total RNA was isolated from cells on the scaffolds using the Trizol reagent (Sangon Biotech, China). The RT-qPCR protocol was implemented using a specialized PCR kit designed for streamlining the one-step method. The expression analysis was performed on a PCR platform (LightCycler 480, Roche, Switzerland), which allowed for precise quantification of the gene transcripts. The relative expression levels of the target genes were calculated using the comparative Ct ($2^{-\Delta\Delta Ct}$) method. This approach involved normalizing the expression of the genes of interest against the endogenous control, glyceraldehyde-3-phosphate dehydrogenase (*Gapdh*), to account for variations in RNA amounts and to ensure accurate comparison of expression levels across samples. The primer sequences utilized for the amplification of the target and reference genes were thoroughly listed in Table 1, facilitating transparency and reproducibility of the results.

## Statistical Analysis

All the Statistical analysis were carried out using the prism 9.0.0 (GraphPad software, USA). All data are expressed as the mean ± standard deviation (SD). Shapiro–Wilk test was used to test normality of data. For the analysis of the length-width ratio of hADSCs, an unpaired *t*-test with Welch's correction was utilized. Data of CCK-8 and ALP were tested by two-way ANOVA test using Geisser-Greenhouse correction, followed by Tukey's test for multiple comparisons. Gene expression data obtained from the RT-qPCR were analyzed using repeated measures one-way ANOVA. The Sidak test was employed for multiple comparisons. Other data were carried out by means of Brown-Forsythe and Welch one-way ANOVA test, followed by Dunnett T3 test for multiple comparisons. A p value less than 0.05 was considered statistically significant.

# Results

Two types of scaffolds were fabricated: a bare PCL scaffold without further modification and a surface-modified scaffold processed through multiple steps. The scaffolds were designed with two distinct regions: a tendon-like area with aligned fibers and a bone-like area with orthogonally arranged fibers. To demonstrate the enhanced tendon-bone regeneration capacity of the multi-step processed scaffolds, results were presented in a comparative manner between the unmodified and modified surfaces. Each scaffold, comprising two regions, allowed for two sets of comparisons: the bare fibers versus collagen type I-coated fibers in the aligned region, and the bare fibers versus collagen type I-coated and subsequently

**Table 1** Primer Sequences for RT-qPCR

| Gene Symbol | Genbank ID | Primer Sequences (5′ to 3′) |
|---|---|---|
| *Scx* | NM_001080514.3 | F: CGAGAACACCCAGCCCAAACAG<br>R: CTGTCTTTCTGTCGCGGTCCTTG |
| *Tnc* | NM_001410991.1 | F: TAGTGAAAAACAATACCCGGGG<br>R: TGACATCTTTCACCTCGATCTG |
| *Tnmd* | NM_022144.3 | F: AATATTCAGAAGCGGAAATGGC<br>R: ACATTTTTGAAGACCCACGAAG |
| *Runx2* | NM_001015051.4 | F: AGGCAGTTCCCAAGCATTTCATCC<br>R: TGGCAGGTAGGTGTGGTAGTGAG |
| *Ocn* | NM_199173.6 | F: AGGGCAGCGAGGTAGTGAAGAG<br>R: GGTCAGCCAACTCGTCACAGTC |
| *Col1a1* | NM_000088.4 | F: AAGGTGTTGTGCGATGACG<br>R: TGGTCGGTGGGTGACTCTG |
| *Gapdh* | NM_001256799.3 | F: AATGGGCAGCCGTTAGGAAA<br>R: GCCCAATACGACCAAATCAGAG |

mineralized fibers in the orthogonal region. These outcomes were presented in the form of four groups of data, denoted as aligned (A), aligned + Col1 (A+C), orthogonal (O), and orthogonal + mineralized (O+M).

## Characterization of the Scaffolds

Frontal and lateral representations of the scaffold are depicted in Figure 2A and B, respectively. SEM facilitated the examination of the nanofiber microstructure within the scaffolds. The unaltered fibers displayed a smooth exterior as seen in Figure 2C and D, with fiber diameters measuring 5.3 ± 1.3 μm and skeleton diameters at 281 ± 11.2 μm. Upon Col1 coating, the fibers developed a corrugated morphology (Figure 2E) and an increased diameter of 7.4 ± 2.7 μm. Fibers that underwent mineralization demonstrated the presence of hydroxyapatite particles (Figure 2F) and further increased in diameter to 12.2 ± 1.4 μm. The micrograph demonstrates a uniform coating of Col1 (Figure 2G) and hydroxyapatite (Figure 2H) across the scaffold.

The OrientationJ plug-in for ImageJ was employed to color-code fibers based on their orientation, as shown in Figure 2I and J. This technique enabled the assessment of fiber alignment, extraction of angular data, and representation of fiber angular distribution on polar coordinates using Origin software (Figure 2K and L). A singular color within the images signified a homogeneous fiber orientation, while the concentrated angular distribution in the polar plots confirmed the uniform distribution of fiber directions. The results confirmed that the fibers in the different scaffold layers were systematically arranged in aligned and orthogonal patterns, in accordance with the designed scaffold regions.

Energy-dispersive X-ray spectroscopy (EDS) was utilized to examine the elemental composition within the scaffold. The graphical data indicated an absence of calcium (Ca) and phosphorus (P) in the surface-modified aligned fiber region (Figure 3A), while an enrichment of these elements was observed in the surface-modified orthogonal fiber region (Figure 3B), consistent with SEM findings. Additionally, the elemental distribution table (Figure 3C and D) displayed the distribution of each element, with the Ca/P ratio for the modified orthogonal fibers approximating 2, reflective of the ratio found in natural human bone.

The scaffold's porosity was estimated by calculating the volume fraction, which was approximately 80%, highlighting its considerable porosity. This level of porosity is indicative of enhanced interconnectivity, capacity for cell loading, and facilitation of cellular migration throughout the scaffold structure.

The hydrophilicity of the scaffolds was assessed using a water contact angle measurement instrument, presented in Figure 4A. The water contact angles for scaffolds with hydroxyapatite and Col1 modifications (O+M) were significantly lower than those

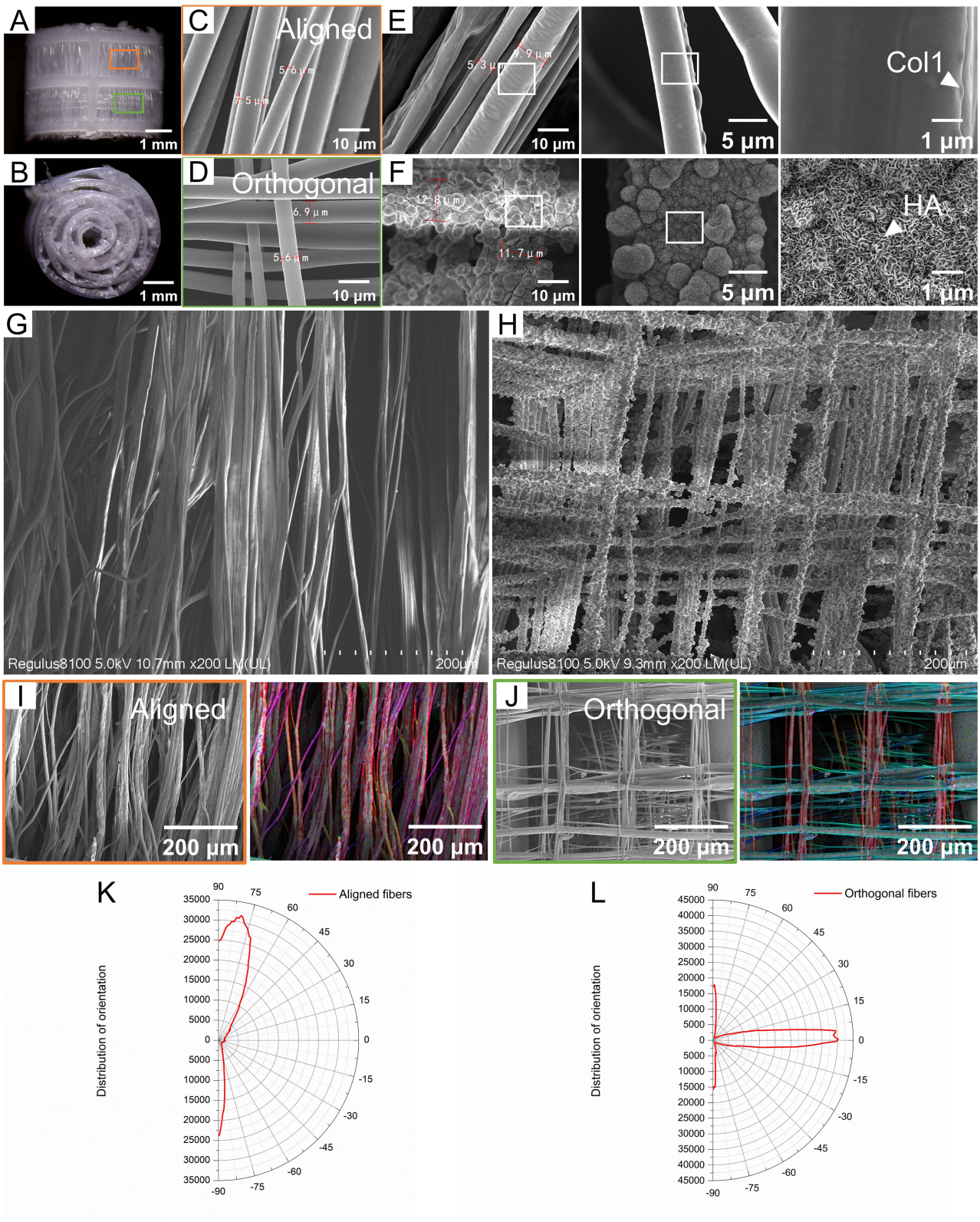


**Figure 2** Characterization of the scaffold. (**A**) Frontal and (**B**) lateral views of the scaffold. (**C**) Unmodified aligned fibers and (**D**) unmodified orthogonal fibers. (**E**) Aligned fibers coated with Col1. (**F**) orthogonal fibers coated with HA. The triangles showed the micro-morphology of Col1 and HA, respectively. (**G** and **H**) Panoramic SEM view of scaffold surface with homogeneous Col1 and HA coating. (**I** and **J**) Fibers marked in different colors indicating different directions. (**K** and **L**) Angle distribution of various fibers shown in polar coordinates.

**Abbreviations**: Col1, type I collagen; HA, hydroxyapatite; SEM, scanning electron microscope.

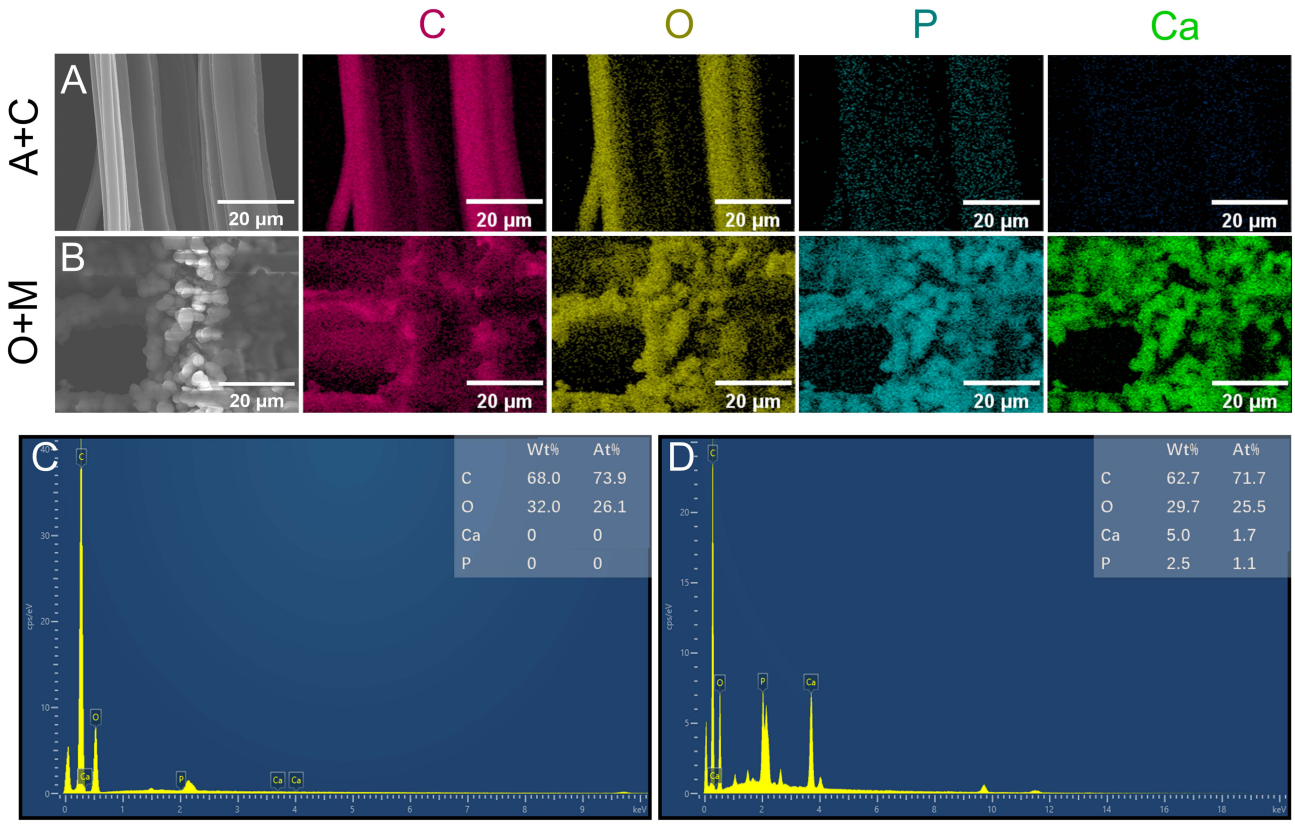


**Figure 3** SEM and EDS mapping images for the A+C group (**A**) and O+M group (**B**). Element distribution table for the A+C group (**C**) and O+M group (**D**).
**Abbreviations**: SEM, scanning electron microscope; EDS, energy dispersive spectroscopy.

modified solely with Col1 (A+C) ($p<0.0001$). Further, the contact angles for Col1 modifications (A+C) were reduced relative to the unmodified surfaces (A and O) ($p<0.0001$). These measurements were repeated three times to ensure accuracy.

Mechanical properties of the scaffolds were evaluated through uniaxial tensile and compression testing, with the resulting stress-strain curves depicted in Figure 4B and C. The curves exhibited a linear elastic region for all test samples. The data highlighted that surface-modified aligned fibers possessed improved tensile properties, whereas the surface-modified orthogonal fibers exhibited better compressive properties. These mechanical characteristics are crucial for ensuring that the scaffolds can withstand physiological loads and provide the necessary support for tissue regeneration.

## Assessment of hADSC Viability and Morphology

hADSCs were utilized to evaluate the cytocompatibility of the scaffolds. Live/dead staining performed at the first and tenth days after seeding revealed substantial hADSC proliferation on all scaffold variations, as evidenced by confocal microscopy images. These images were characterized by a predominance of live cells, indicated by green fluorescence, and a scarcity of dead cells, marked by red fluorescence (Figure 5A). Evaluation of cellular morphology via F-actin staining at days 1 and 10 post-seeding revealed the presence of polygonal cells on orthogonal fibers. In contrast, cells on aligned fibers exhibited an elongated, spindle-like morphology, akin to tendon cells, as depicted in Figure 5B. These morphological characteristics were further confirmed by SEM imaging (Figure 5C). The aspect ratio of cells on aligned fibers was significantly higher than that of cells on orthogonal fibers ($p=0.0002$) (Figure 5D), suggesting that cells exhibit distinct morphologies based on the orientation of the adhesive substrate. These measurements were repeated three times to ensure accuracy.

The dynamics of cell proliferation were quantified using the Cell Counting Kit-8 (CCK-8) assay (Figure 5E). The assay results at days 1, 3, and 7 post-seeding revealed a consistent increase in cell proliferation across all groups of scaffolds. The optical density (OD) values for cells on the mineralized areas (Group O+M) were significantly higher than

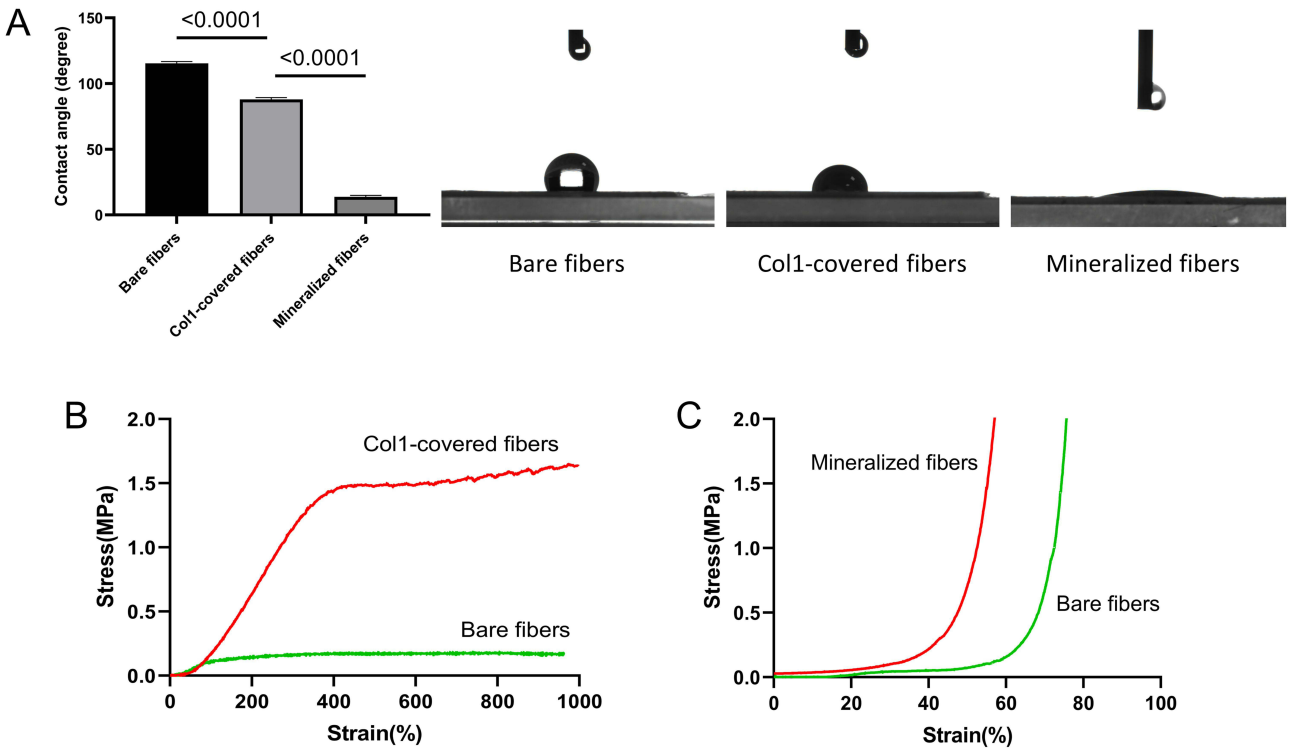


**Figure 4** (**A**) Water contact angles of unmodified and modified scaffolds (n=3). (**B**) Tensile tests of scaffolds coated with Col I versus unmodified scaffolds. (**C**) Compression tests of scaffolds coated with HA versus unmodified scaffolds.
**Abbreviations**: Col I, type I collagen; HA, hydroxyapatite.

those on the areas with bare fibers (Group O) at day 3 (p=0.0252) and day 7 (p=0.0183). No significant differences were observed among the other groups. These measurements were repeated three times to ensure accuracy.

## Differentiation of hADSCs

The mineralization of the extracellular matrix (ECM) serves as an indicator of osteoblastic differentiation within cells. Alizarin Red S staining, a technique to identify bone-like ECM deposits, was implemented to investigate the level of ECM mineralization by hADSCs within the scaffold constructs (Figure 6A). Within the aligned (A) and collagen-coated aligned (A+C) groups, distinct regions of red staining were not evident, indicating minimal mineral deposition. In comparison, the orthogonal (O) group displayed a modest presence of red spots. Notably, the orthogonal with mineralization (O+M) group exhibited extensive red staining areas, which not only covered the fiber surfaces but also filled the spaces between fibers.

ALP is recognized as an early marker of osteogenic differentiation, with a critical function in the preparation of ECM mineral deposits. Scaffolds from each experimental group underwent staining with the azo coupling method to visualize ALP activity (Figure 6B). Areas displaying ALP activity were identified by blue-purple staining on the scaffolds. The O+M group exhibited notably larger areas of blue staining compared to the orthogonal (O) group, suggesting higher ALP activity. In contrast, the A and A+C groups showed less pronounced blue staining, indicating lower levels of ALP activity. A SEM image of the O+M group revealed calcium salt deposits within the cells (Figure 6C), which is consistent with osteogenic activity.

The semi-quantitative analysis of Alizarin Red S staining supported the visual findings. Comparative analysis among the groups demonstrated that the O+M group had significantly greater Alizarin Red S staining intensity compared to the O group (p=0.002), and the staining in the O group was higher than that in the A group (p=0.038) (Figure 6D). Between the A and A+C groups, no significant difference was observed (p>0.05). These measurements were repeated three times to ensure accuracy.

Quantitative ALP assays further substantiated these findings (Figure 6E). The O+M group demonstrated significantly higher ALP activity compared to the O group at both day 14 (p=0.0326) and day 28 (p<0.0001). Additionally, the

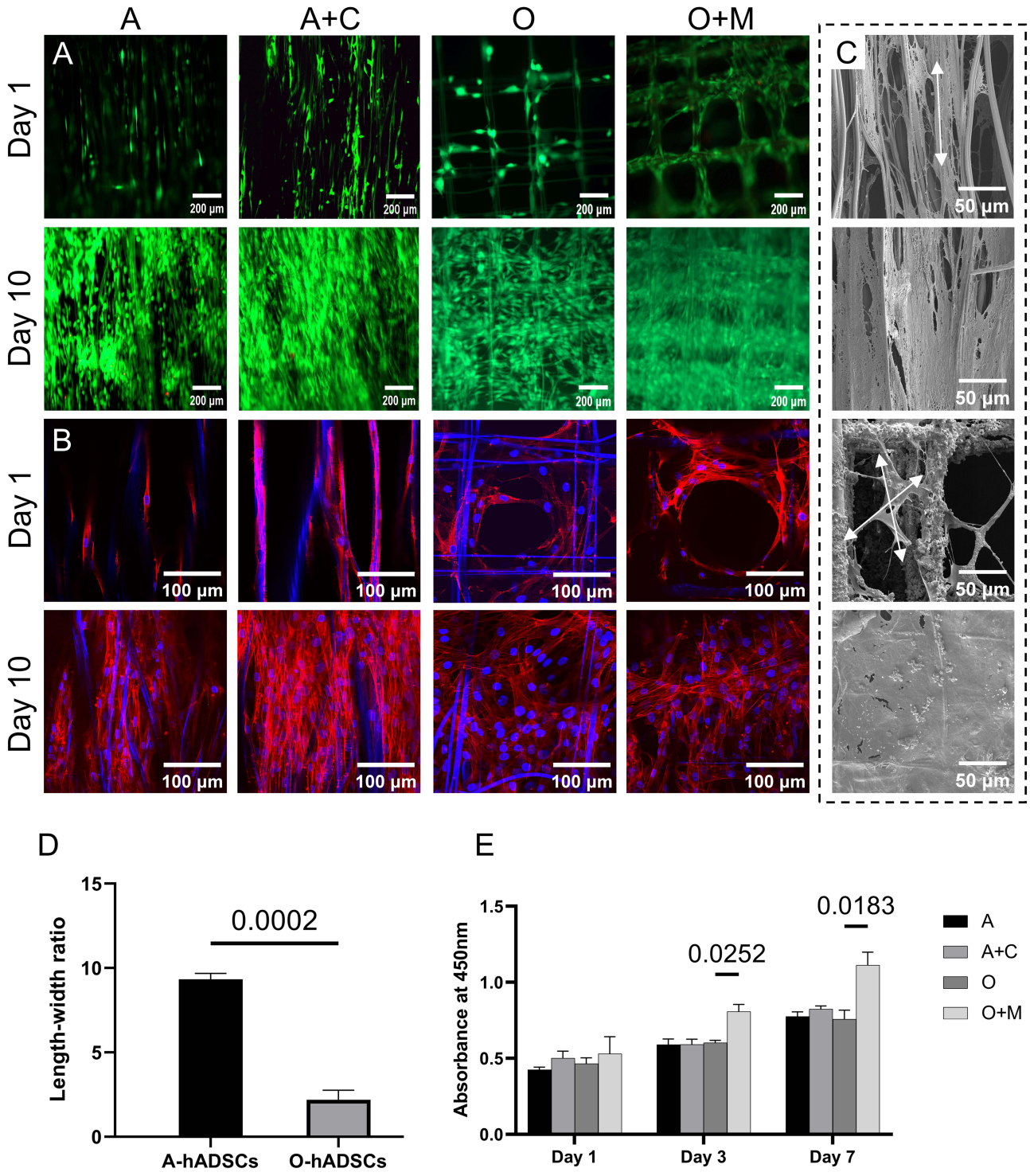


**Figure 5** (**A**) Live/Dead staining on day 1 and day 10. (**B**) Phalloidin staining on day 1 and day 10. (**C**) Morphological presentation of hADSCs on aligned and orthogonal fibers. The arrows showed the cells were spindle-shaped on aligned fibers while polygonal on orthogonal fibers. (**D**) Ratio of the longest to shortest diameter of hADSCs on aligned and orthogonal fibers (n=3). (**E**) Proliferation of hADSCs tested using CCK-8 assay (n=3).
**Abbreviations**: hADSCs, human adipose-derived stem cells; CCK-8, cell counting kit-8.

O group exhibited greater ALP activity than the A group at day 28 (p=0.0246), although no significant difference was observed at day 14 (p>0.05). These measurements were repeated three times to ensure accuracy. These results suggest that the mineralized scaffolds in the O+M group are more conducive to osteogenic differentiation and ECM mineralization, as evidenced by the increased ALP activity and subsequent calcium salt deposition.

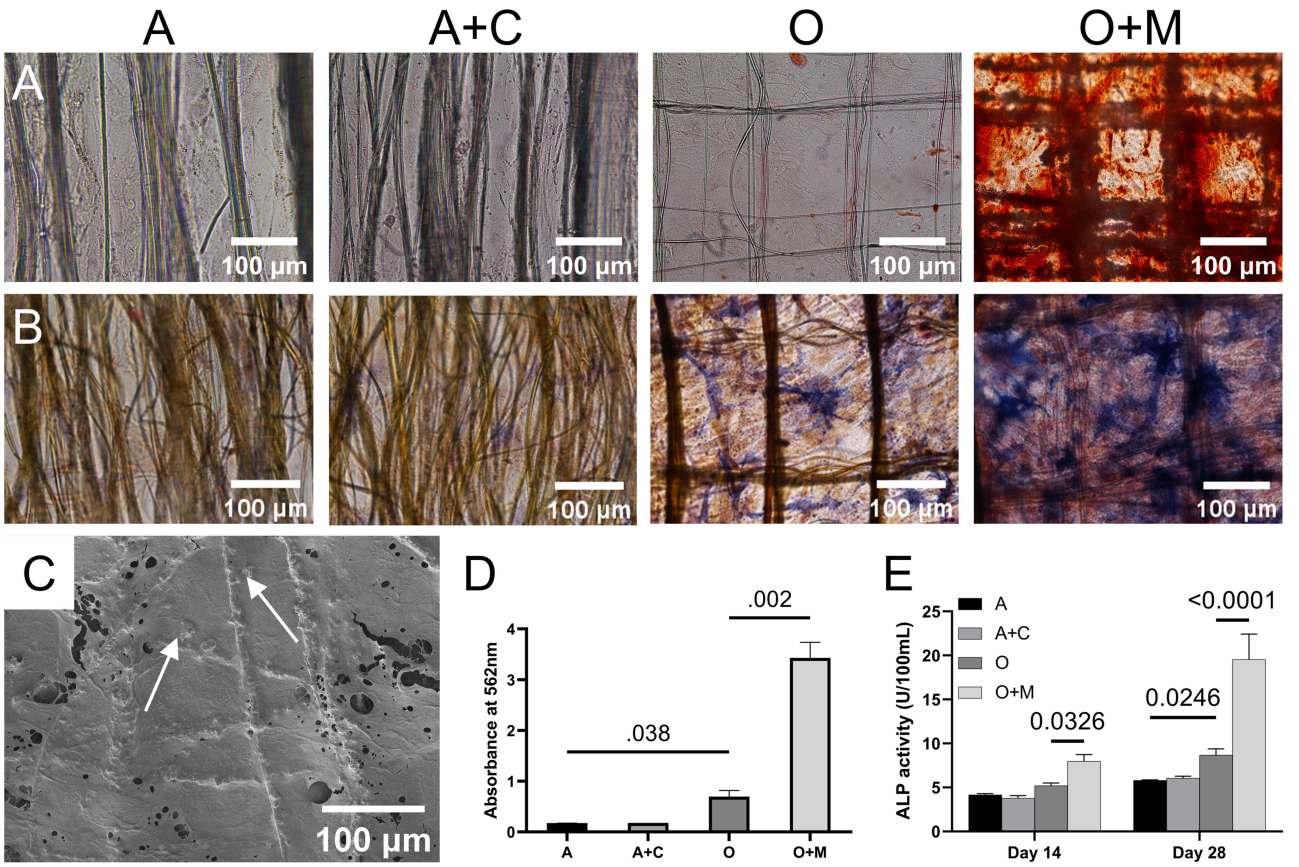


**Figure 6** (**A**) Alizarin Red staining for detecting calcium salt deposition in the ECM of hADSCs. (**B**) Azo coupling method for ALP staining in hADSCs. (**C**) SEM image of the O+M group showed calcium salt deposition. (**D**) Semi-quantitative analysis of Alizarin Red staining (n=3). (**E**) ALP activity assay at day 14 and day 28 (n=3).
**Abbreviations**: ECM, extracellular matrix; hADSCs, human adipose-derived stem cells; ALP, alkaline phosphatase; SEM, scanning electron microscope.

Col1 predominates in the extracellular matrix of tendon and bone tissues. There is an observed upregulation of Col1 expression when stem cells undergo differentiation into these tissue types. To evaluate the Col1 expression in the scaffold cells across the different groups, an immunostaining technique was employed, as illustrated in Figure 7A. The photos indicate that all four groups exhibited Col1 expression within their scaffold cells. Notably, the expression levels of Col1 in cells from group O+M were more pronounced than in group O (P=0.006). Col1 in Group A+C is more than that in Group A by comparing the mean intensity of fluorescence, however with no significant difference (p>0.05) (Figure 7B). These measurements were repeated three times to ensure accuracy.

Runx2 serves as an early indicator of osteogenic differentiation, while SCX and TNC are recognized as specific markers for tendon lineage. Immunostaining for these proteins was employed to investigate the tendencies for tenogenic and osteogenic differentiation of hADSCs amongst the scaffold groups. The Runx2 expression in group O+M was significantly higher than that in group O (Figure 7C). Semi-quantitative analysis of immunofluorescence revealed a clear distinction in Runx2 levels between the O and O+M groups (p=0.027) (Figure 7D). These measurements were repeated three times to ensure accuracy.

In contrast to group A, samples from group A+C exhibited elevated expression levels of SCX and TNC, as indicated in Figure 8A and B. Immunofluorescence semi-quantitative analysis corroborated these observations, with SCX demonstrating a significant increase (p=0.015) and TNC also showing a significant upregulation (p=0.042), detailed in Figure 8C and D. Furthermore, the tenascin-C level in the combined Group A+C was significantly higher than that in Group A alone (p=0.002). Although the mean expression level of SCX in Group A+C was greater than in Group A, this elevation did not achieve statistical significance (p>0.05). These measurements were repeated three times to ensure accuracy.

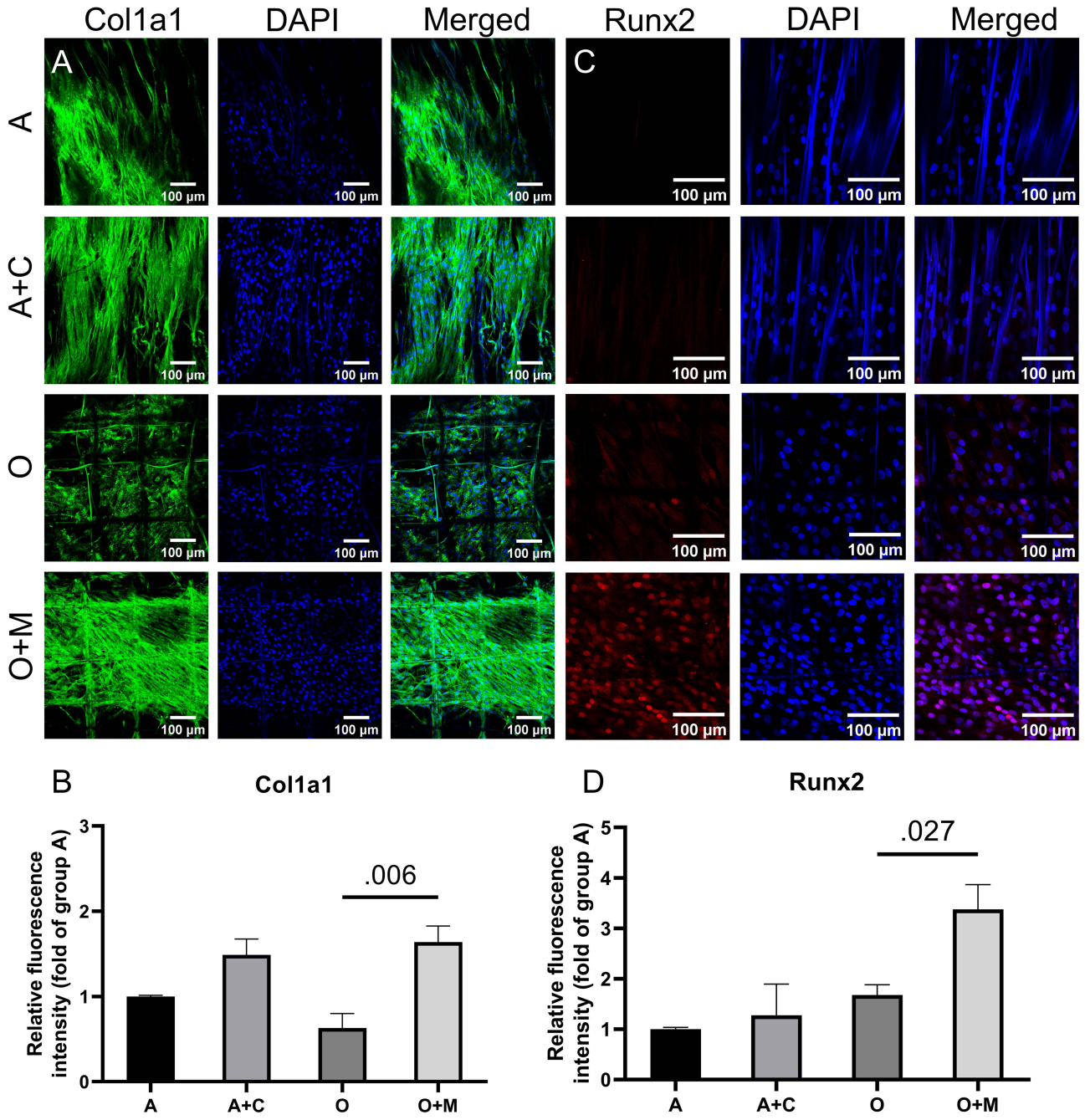


**Figure 7** (**A**) Col1a1 immunofluorescence staining in cells on scaffolds. (**B**) Immunofluorescence semi-quantitative analysis of Col1a1 (n=3). (**C**) Runx2 immunofluorescence staining in cells on scaffolds. (**D**) Immunofluorescence semi-quantitative analysis of Runx2 (n=3).

RT-qPCR analysis revealed that Group A+C exhibited a higher expression of tenogenic genes, specifically *Scx* (p=0.029), *Tnmd* (p<0.001), and *Tnc* (p<0.001), compared to Group A, as illustrated in Figure 9A–C. Regarding osteogenic gene expression, Group O+M showed increased levels of *Col1a1* compared to Group O (p=0.009), depicted in Figure 9D, and exhibited enhanced expression of *Ocn* relative to Group O (p=0.01), shown in Figure 9E. While the expression of *Runx2* in Group O+M was higher than in Group O, the difference was not statistically significant (p>0.05), as presented in Figure 9F. Additionally, *Runx2* expression was found to be higher in Group O compared to Group A (p=0.014). The results also indicated that *Col1a1* expression in Group A+C exceeded that of Group A (p=0.005). These measurements were repeated three times to ensure accuracy.

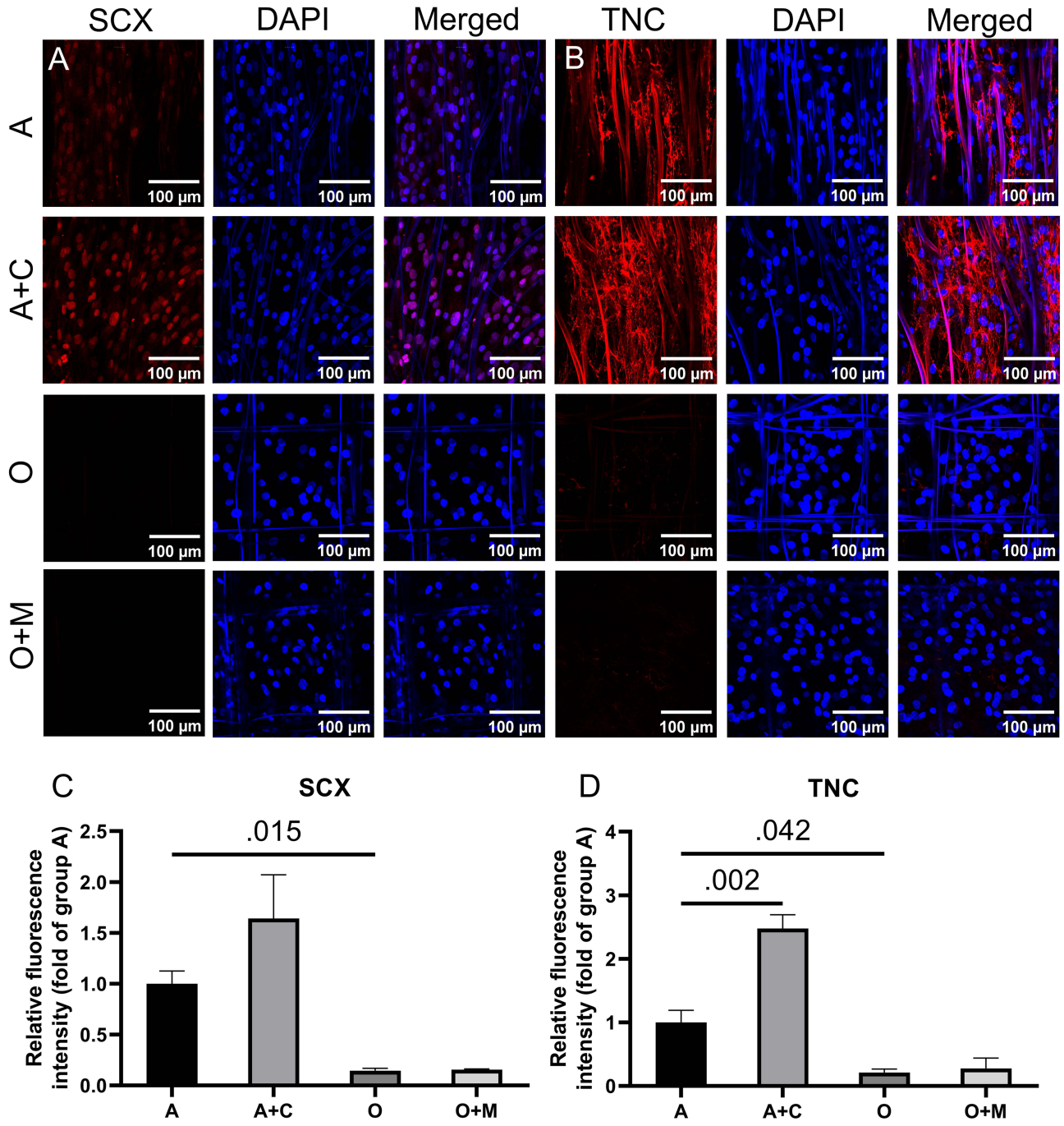


**Figure 8** (**A**) SCX immunofluorescence staining in cells on scaffolds. (**B**) TNC immunofluorescence staining in cells on scaffolds (n=3). (**C**) Immunofluorescence semi-quantitative analysis of SCX. (**D**) Immunofluorescence semi-quantitative analysis of TNC (n=3).

## Discussion

Conventional electrospinning of PCL typically results in scaffolds with pore sizes that are not suitable for cell migration. In contrast, MEW techniques with PCL can produce scaffolds with customizable pore sizes and structured designs that are beneficial for guiding the orderly arrangement and spread of cells.[23] This attribute is crucial for facilitating the concurrent healing of tendon and bone tissues. To compensate for the low mechanical strength of MEW-fabricated structure, FDM technology is employed to construct a framework for the MEW membrane. Further structural design transforms the two-dimensional membrane into a curled, cylindrical three-dimensional scaffold, enhancing mechanical

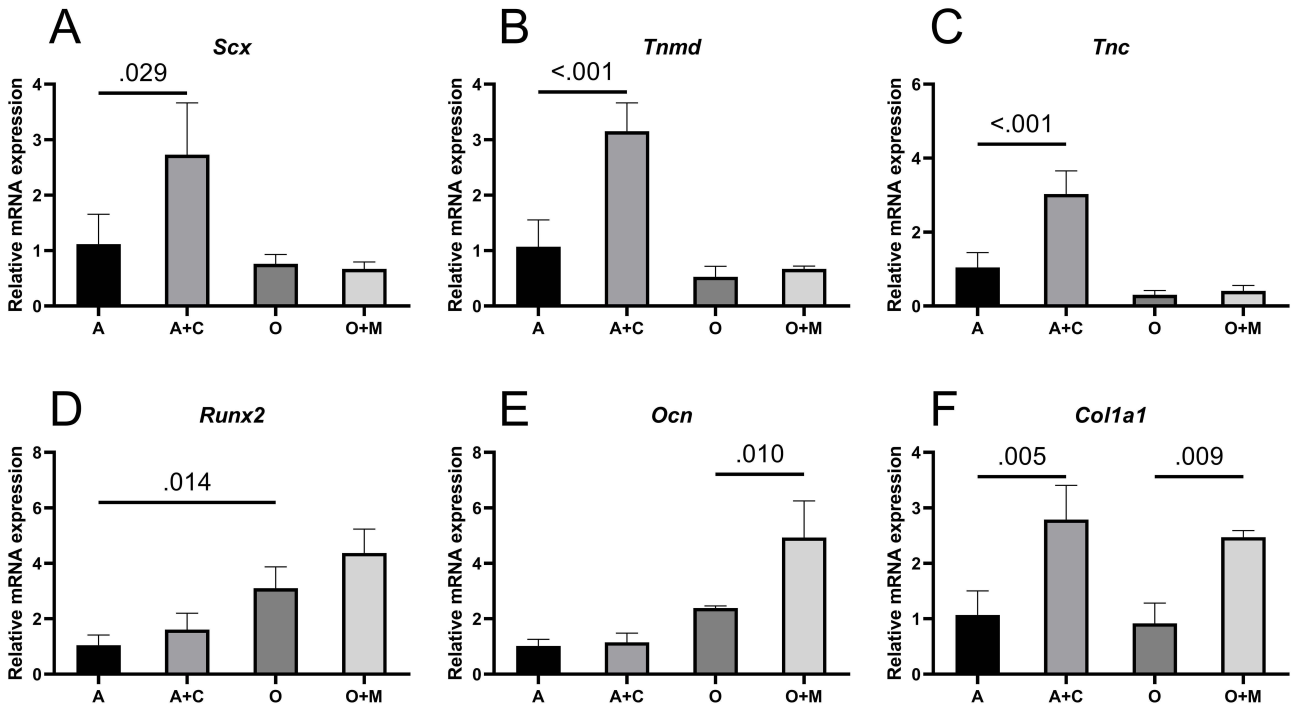


**Figure 9** Expression analysis of tendon-specific genes *Scx* (**A**), *Tnmd* (**B**) and *Tnc* (**C**), osteogenic related genes *Col1a1* (**D**) and *Ocn* (**E**), and *Runx2* (**F**) of hADSCs in different scaffolds (n=3).
**Abbreviations**: hADSCs, human adipose-derived stem cells.

properties. Beyond structural design, considerations for cell affinity and differentiation are integrated to create a biomimetic, cell-friendly scaffold for tendon-bone interface regeneration. The scaffold's structure and mechanical properties are tested, coupled with in vitro cell culture and assessment of tenogenic and osteogenic potential. This biomimetic scaffold holds the potential for osteotendinous junction regeneration, offering a prospective treatment approach for integrated tendon-bone repair in clinical settings.

The present investigation utilized the sophisticated capabilities of MEW technology to exert precise control over the structure and inter-fiber spacing of the fabricated scaffolds. The architectural design of the scaffold was carefully crafted to emulate the natural organization of the tendon-bone junction. The resultant scaffold featured a stratified structure, with fiber spacings tailored to the diameter of collagen fiber bundles in tendons, the optimal pore size for osteogenesis, and the dimensions of resident cells. A PCL hybrid layer comprising microfibers coupled with a coarse fiber exoskeleton was fabricated using three-dimensional printing techniques. This hybrid structure was further functionalized with primary extracellular matrix constituents, Col1 and hydroxyapatite, representative of tendon and bone matrices, respectively. The engineered composite layers were meticulously assembled into a cylindrical, three-dimensional scaffold under stereoscopic visualization. Characterization of these scaffolds revealed a complex, layered architecture and composition that closely mirrors the extracellular matrix environment of native tendon and bone tissues.

While mechanical strength is crucial for tendon or bone substitutes,[26] it is less critical for scaffolds that serve as bridges. To clearly observe the mechanical changes in modified fibers, the coarse fiber framework was removed during testing. Tensile and compressive tests on aligned and crossed fibers showed that modified fibers had a significantly higher elastic modulus, as indicated by the slope of the curve. During compression testing, the slope increased as the scaffold densified into a solid structure due to pore collapse under pressure, enhancing compressive strength. The scaffold developed in this study is intended to bridge the tendon-bone interface. Surface modification improved mechanical properties, but the key advancement was altering the extracellular matrix environment. The scaffold's tensile and compressive strength is lower than that of natural tissue,[27] thus is only suitable for tension-free tendon-bone attachment repairs.

The advent of biodegradable, biomimetic scaffolds produced via 3D printing has notably advanced the field of tendon and bone tissue engineering. Xi et al developed a multi-layered scaffold utilizing 3D printing methods aimed at treating injuries of the rotator cuff.[28] Nevertheless, the constraints of simple extrusion-based printing precluded the generation of fibers within the nano-microscale range. In contrast, electrospinning technology is proficient in fabricating fibers of nanoscale diameters, adeptly mimicking the extracellular matrix of tendons, thereby holding substantial promise for the creation of scaffolds that enhance tendon repair. For instance, Lin et al crafted a scaffold from PCL nanofiber film amalgamated with collagen type I through conventional electrospinning, which proved to facilitate osteogenic differentiation in tendon stem/progenitor cells (TSPCs).[19] Additionally, Wen et al produced an aligned nanofiber film scaffold by augmenting the collector's rotational speed during the electrospinning process.[29] They employed a gradient deposition of hydroxyapatite via the hydroxyapatite precipitation method, which was shown to encourage osteogenic differentiation in adipose-derived stem cells. However, these scaffolds are not without their limitations, including a singular structural form, inadequate porosity, and the absence of a three-dimensional aspect, all of which limit their capability to concurrently address the repair needs of both tendon and bone tissues. The current study applied the more sophisticated MEW technology, affording meticulous control over fiber deposition and inter-fiber spacing. The integration of MEW technology with 3D printing significantly augmented the mechanical strength of the scaffold. This collaborative strategy resulted in the creation of a biomimetic scaffold with a stratified structure that emulates the layered organization of native tissue matrices.

The structural morphology of scaffolds markedly impacts cellular behavior and is crucial for directing cell physiology and differentiation pathways. Zhang et al found that mesenchymal stem cells exhibited a tendency to differentiate towards tendon lineage on unidirectionally aligned fibers, whereas a random fiber alignment favored osteogenic differentiation.[30] In the current study, the engineered scaffolds incorporated both aligned and orthogonal fibers. Cells cultured on these scaffolds assumed distinct morphologies: on the aligned fibers, cells extended along the fiber direction, adopting elongated, spindle-like shapes characteristic of fibroblasts; conversely, cells on the orthogonal fibers displayed a random arrangement with more polygonal geometries. This stratified architecture of the scaffold permitted stem cells to undergo multidirectional differentiation within the same construct. The osteogenic potential of the O+M scaffold was underscored by the results of Alizarin Red S staining and Alkaline phosphatase activity assays, which indicated a pronounced enhancement in ECM mineralization and osteoblastic activity within hADSCs. This suggests that the tailored design and mineralization process of the scaffold significantly foster bone tissue formation. Complementary to these findings, immunofluorescence staining and RT-qPCR analyses provided evidence that the regions of the scaffold with unidirectionally aligned fibers promoted tenogenic differentiation, whereas the sections with orthogonal fiber alignment facilitated osteogenic differentiation of stem cells. These observations are in agreement with established research, reinforcing the concept that scaffold architecture plays a fundamental role in directing stem cell fate.[31–33]

While reducing scaffold fiber size to microscale or even nanoscale dimensions can enhance cell adhesion, additional measures have been taken to augment the cell adhesiveness of PCL by surface modification, due to its inherent hydrophobicity that is detrimental to stem cell attachment. The surface modification aimed to amplify the hydrophilicity of the scaffold and bolster cell adhesion, without impeding cellular differentiation processes. The modification involved the application of Col1 to the aligned fibers, with the orthogonal fibers receiving a coating of Col1 followed by mineralization with hydroxyapatite. The scaffold's pore size is a critical factor influencing cell migration, proliferation, and infiltration, all of which are pivotal for the successful application of the scaffold.[34,35] The scaffold fabricated in this study featured a high level of porosity, with pore dimensions tailored to the diameter of tendon collagen fiber bundles and the optimal conditions for bone regeneration. This design not only ensured sufficient space for cell adhesion and movement but also directed the organization of collagen, which is advantageous for stem cell growth and differentiation. Results from immunofluorescence staining and RT-qPCR indicated that gene expression associated with tendon differentiation was higher in stem cells cultured on the Col1-modified aligned fiber scaffold compared to the unmodified version. This outcome may be ascribed to Col1's role in enhancing cellular adhesion and proliferation, promoting the synthesis of Col1 within cells, and catalyzing the differentiation process.

Local mineral density and substrate rigidity play pivotal roles in the differentiation of stem cells. It is recognized that tendon cells are typically situated within pliable collagen fibers, while osteocytes flourish within the stiffer, mineral-rich matrix. To replicate these distinct environmental conditions, mineralization was performed on the orthogonal fiber region

of the scaffold, thereby manipulating mineral content and substrate stiffness accordingly. Mechanical assays confirmed that the rigidity of the mineralized fibers was substantially greater than that of their non-mineralized counterparts. Furthermore, increasing evidence has demonstrated that the integration of hydroxyapatite nanoparticles within scaffolds can enhance the osteogenic differentiation of stem cells.[26,36] Consequently, the mineralization of the orthogonal fibers in the scaffold designed for this study was posited to more effectively foster osteogenic differentiation in hADSCs, a notion substantiated by immunofluorescence staining and RT-qPCR analysis, revealing an upregulation in osteogenic markers.

The present study is not without its limitations. The fabrication process of the scaffold involves manual techniques, which presents a challenge to upscale production for industrial applications. Variability between batches due to these manual processes may influence experimental outcomes. Furthermore, the scaffold's design was tailored to foster osteogenic and tenogenic differentiation, with no consideration given to chondrogenic differentiation pathways. While the incorporation of coarse PCL fibers into the scaffold's architecture improved its structural integrity, allowing it to retain a three-dimensional form, there were notable changes in fiber morphology upon immersion in culture media. The mechanical properties of the scaffold, though improved, still fall short when compared to native tendon and bone tissues, limiting its use in vivo primarily to that of a bridging material, rather than a stand-in for temporary tissue replacement. Additionally, the long biodegradation period of PCL and its variable degradation rate under different biological conditions necessitate a thorough examination of the scaffold's degradation behavior within a living organism. The underlying mechanisms by which the biomimetic scaffold enhances osteogenic and tenogenic differentiation of hADSCs remain unexplored in this study. Future research will be required to tackle these challenges. In subsequent studies, appropriate animal models will be selected to assess the efficacy of the biomimetic scaffold in promoting tendon-bone integration and healing in vivo.

## Conclusion

In conclusion, a hierarchical biomimetic scaffold, mirroring the complex architecture of the tendon-bone interface, has been successfully engineered. Utilizing the precision of MEW technology, the scaffold featured controlled fiber diameters, patterns, and spacings, which permitted the fabrication of a stratified structure in an integrated manner. The incorporation of coarse PCL fibers ensured the maintenance of a three-dimensional shape and high porosity, addressing the shortcomings of conventional electrospinning processes that produce monolithic and less porous structures. The scaffold's distinctive regions effectively directed stem cell fate, orchestrated collagen fiber orientation, and promoted cellular differentiation. The aligned fibers received a coating of Col1, while the orthogonal fibers were enhanced with hydroxyapatite, thereby augmenting the scaffold's biomimetic qualities, hydrophilicity, and capacity to induce differentiation. In vitro assessments revealed that hADSCs exhibited a propensity to differentiate along distinct pathways within the varying structural zones of the scaffold, with more marked effects observed on the surface-modified regions compared to the unmodified ones. This investigation has introduced an innovative approach in tissue engineering, presenting a viable strategy for localized induction of cell differentiation. It holds significant potential for facilitating direct tendon-bone healing, thus laying the groundwork for the future clinical deployment of tissue engineering scaffolds.

## Acknowledgments

This work was financially supported by the National Natural Science Foundation of China (81972042, 82072400), the Natural Science Foundation of Jiangsu Province (BK20200001, BE2019736, and BE2019679).

## Disclosure

The authors report no conflicts of interest in this work.

## References

1. Briggs AM, Cross MJ, Hoy DG, et al. Musculoskeletal health conditions represent a global threat to healthy aging: a report for the 2015 World Health Organization world report on ageing and health. *Gerontologist*. 2016;56(Suppl 2):S243–55. doi:10.1093/geront/gnw002
2. Millar N, Silbernagel KG, Thorborg K, et al. Tendinopathy. *Nature Reviews. Disease Primers*. 2021;7(1):1. doi:10.1038/s41572-020-00234-1
3. Dang A, Davies M. Rotator cuff disease: treatment options and considerations. *Sports Med Arthrosc Rev*. 2018;26(3):129–133. doi:10.1097/JSA.0000000000000207

4. Vitale MA, Vitale MG, Zivin JG, et al. Rotator cuff repair: an analysis of utility scores and cost-effectiveness. *J Shoulder Elbow Surg*. 2007;16 (2):181–187. doi:10.1016/j.jse.2006.06.013
5. Lu HH, Thomopoulos S. Functional attachment of soft tissues to bone: development, healing, and tissue engineering. *Annu Rev Biomed Eng*. 2013;15(1):201–226. doi:10.1146/annurev-bioeng-071910-124656
6. Shaw H, Benjamin M. Structure-function relationships of entheses in relation to mechanical load and exercise. *Scand J Med Sci Sports*. 2007;17 (4):303–315. doi:10.1111/j.1600-0838.2007.00689.x
7. Genin G, Kent A, Birman V, et al. Functional grading of mineral and collagen in the attachment of tendon to bone. *Biophys J*. 2009;97(4):976–985. doi:10.1016/j.bpj.2009.05.043
8. Derwin K, Galatz LM, Ratcliffe A, et al. Enthesis repair: challenges and opportunities for effective tendon-to-bone healing. *J Bone Joint Surg Am*. 2018;100(16):e109. doi:10.2106/JBJS.18.00200
9. Lu H, Chen C, Xie S, et al. Tendon healing in bone tunnel after human anterior cruciate ligament reconstruction: a systematic review of histological results. *J Knee Surg*. 2019;32(5):454–462. doi:10.1055/s-0038-1653964
10. Rodeo S, Arnoczky SP, Torzilli PA, et al. Tendon-healing in a bone tunnel. A biomechanical and histological study in the dog. *J Bone Joint Surg Am*. 1993;75(12):1795–1803. doi:10.2106/00004623-199312000-00009
11. Kuang G, Yau WP, Lu WW, et al. Osteointegration of soft tissue grafts within the bone tunnels in anterior cruciate ligament reconstruction can be enhanced. *Knee Surg Sports Traumatol Arthrosc*. 2010;18(8):1038–1051. doi:10.1007/s00167-009-0910-1
12. Shojaee A, Parham A. Strategies of tenogenic differentiation of equine stem cells for tendon repair: current status and challenges. *Stem Cell Res Ther*. 2019;10(1):181. doi:10.1186/s13287-019-1291-0
13. Hanselman AE, Lalli TAJ, Santrock RD. Topical review: use of fetal tissue in foot and ankle surgery. *Foot Ankle Spec*. 2015;8(4):297–304. doi:10.1177/1938640015578513
14. Galatz L, Gerstenfeld L, Heber-Katz E, et al. Tendon regeneration and scar formation: the concept of scarless healing. *J Orthop Res*. 2015;33 (6):823–831. doi:10.1002/jor.22853
15. Beredjiklian P, Favata M, Cartmell JS, et al. Regenerative versus reparative healing in tendon: a study of biomechanical and histological properties in fetal sheep. *Ann Biomed Eng*. 2003;31(10):1143–1152. doi:10.1114/1.1616931
16. Gimble JM. Adipose tissue-derived therapeutics. *Expert Opin Biol Ther*. 2003;3(5):705–713
17. Gui-Bo Y, You-Zhu Z, Shu-Dong W, et al. Study of the electrospun PLA/silk fibroin-gelatin composite nanofibrous scaffold for tissue engineering. *J Biomed Mater Res A*. 2010;93(1):158–163. doi:10.1002/jbm.a.32496
18. Li X, Xie J, Lipner J, et al. Nanofiber scaffolds with gradations in mineral content for mimicking the tendon-to-bone insertion site. *Nano Letters*. 2009;9(7):2763–2768. doi:10.1021/nl901582f
19. Lin Y, Zhang L, Liu NQ, et al. In vitro behavior of tendon stem/progenitor cells on bioactive electrospun nanofiber membranes for tendon-bone tissue engineering applications. *Int J Nanomedicine*. 2019;14:5831–5848. doi:10.2147/IJN.S210509
20. Zhu C, Pongkitwitoon S, Qiu J, et al. Design and fabrication of a hierarchically structured scaffold for tendon-to-bone repair. *Adv Mater*. 2018;30 (16):e1707306. doi:10.1002/adma.201707306
21. Matsumoto T, Sato Y, Kobayashi T, et al. Adipose-derived stem cell sheets improve early biomechanical graft strength in rabbits after anterior cruciate ligament reconstruction. *Am J Sports Med*. 2021;49(13):3508–3518. doi:10.1177/03635465211041582
22. Madhurakkat Perikamana S, Lee J, Ahmad T, et al. Harnessing biochemical and structural cues for tenogenic differentiation of adipose derived stem cells (ADSCs) and development of an in vitro tissue interface mimicking tendon-bone insertion graft. *Biomaterials*. 2018;165:79–93. doi:10.1016/j.biomaterials.2018.02.046
23. Kade J, Dalton PD. Polymers for melt electrowriting. *Adv Healthc Mater*. 2021;10(1):e2001232. doi:10.1002/adhm.202001232
24. Orr S, Chainani A, Hippensteel KJ, et al. Aligned multilayered electrospun scaffolds for rotator cuff tendon tissue engineering. *Acta biomaterialia*. 2015;24:117–126. doi:10.1016/j.actbio.2015.06.010
25. Sun Y, Han F, Zhang P, et al. A synthetic bridging patch of modified co-electrospun dual nano-scaffolds for massive rotator cuff tear. *J Mater Chem B*. 2016;4(45):7259–7269. doi:10.1039/c6tb01674j
26. Zhao C, Wang X, Gao L, et al. The role of the micro-pattern and nano-topography of hydroxyapatite bioceramics on stimulating osteogenic differentiation of mesenchymal stem cells. *Acta biomaterialia*. 2018;73:509–521. doi:10.1016/j.actbio.2018.04.030
27. LaCroix A, Duenwald-Kuehl SE, Lakes RS, et al. Relationship between tendon stiffness and failure: a metaanalysis. *J Appl Physiol*. 2013;115 (1):43–51. doi:10.1152/japplphysiol.01449.2012
28. Jiang X, Wu S, Kuss M, et al. 3D printing of multilayered scaffolds for rotator cuff tendon regeneration. *Bioactive Materials*. 2020;5(3):636–643. doi:10.1016/j.bioactmat.2020.04.017
29. Liu W, Lipner J, Xie J, et al. Nanofiber scaffolds with gradients in mineral content for spatial control of osteogenesis. *ACS Appl Mater Interfaces*. 2014;6(4):2842–2849. doi:10.1021/am405418g
30. Zhang C, Yuan H, Liu H, et al. Well-aligned chitosan-based ultrafine fibers committed teno-lineage differentiation of human induced pluripotent stem cells for achilles tendon regeneration. *Biomaterials*. 2015;53:716–730. doi:10.1016/j.biomaterials.2015.02.051
31. Tolbert J, French T, Kitson A, et al. Solvent-cast 3D printing with molecular weight polymer blends to decouple effects of scaffold architecture and mechanical properties on mesenchymal stromal cell fate. *J Biomed Mater Res A*. 2024. doi:10.1002/jbm.a.37674
32. Nathan A, Baker BM, Nerurkar NL, et al. Mechano-topographic modulation of stem cell nuclear shape on nanofibrous scaffolds. *Acta biomaterialia*. 2011;7(1):57–66. doi:10.1016/j.actbio.2010.08.007
33. Sands R, Mooney DJ. Polymers to direct cell fate by controlling the microenvironment. *Curr Opin Biotechnol*. 2007;18(5):448–453. doi:10.1016/j.copbio.2007.10.004
34. Kim H, Jung G-Y, Yoon J-H, et al. Preparation and characterization of nano-sized hydroxyapatite/alginate/chitosan composite scaffolds for bone tissue engineering. *Mater Sci Eng C*. 2015;54:20–25. doi:10.1016/j.msec.2015.04.033
35. Screen H, Lee DA, Bader DL, et al. An investigation into the effects of the hierarchical structure of tendon fascicles on micromechanical properties. *Proc Inst Mech Eng H*. 2004;218(2):109–119. doi:10.1243/095441104322984004
36. Zhou K, Yu P, Shi X, et al. Hierarchically porous hydroxyapatite hybrid scaffold incorporated with reduced graphene oxide for rapid bone ingrowth and repair. *ACS nano*. 2019;13(8):9595–9606. doi:10.1021/acsnano.9b04723